

# Traction control design for off-road mobility using an SPH-DAE cosimulation framework

Wei Hu<sup>1</sup> • · Zhenhao Zhou<sup>1</sup> · Samuel Chandler<sup>2</sup> · Dimitrios Apostolopoulos<sup>2</sup> · Ken Kamrin<sup>3</sup> · Radu Serban<sup>1</sup> · Dan Negrut<sup>1</sup> •

Received: 10 October 2021 / Accepted: 28 January 2022 / Published online: 1 March 2022 © The Author(s), under exclusive licence to Springer Nature B.V. 2022

#### Abstract

We describe an analytical framework implemented in a general-purpose mobility simulation platform for enabling the design of control policies for improved rover mobility in granular terrain environments. We employ a homogenization of the granular material and use an elasto-plastic continuum model to capture the dynamics of the deformable terrain. The solution of the continuum problem is obtained using the smoothed particle hydrodynamics method. The Curiosity rover wheel geometry is defined through a mesh. The interaction between each wheel and the granular terrain is handled via cosimulation using so-called boundary conditions enforcing particles attached to the rover wheel. A traction control algorithm is implemented to reduce wheel slip and battery drain in hill-climbing scenario. Several parametric studies are carried out to assess rover simulation robustness for operation in uphill mobility scenario with different heights and friction coefficients. The analysis is carried out in an in-house developed simulation framework called Chrono. The implementation of the methods and models described herein is available on GitHub as open source for free use, modification, and redistribution, as well as reproducibility studies.

**Keywords** Offroad mobility  $\cdot$  Granular material  $\cdot$  Continuum representation  $\cdot$  Smoothed particle hydrodynamics  $\cdot$  Traction control  $\cdot$  Rover dynamics

## 1 Introduction

The problem of a complex mechanical system interacting with granular material is encountered in many engineering terramechanics applications; see, for instance, [1–5]. The discrete element method (DEM) [6], which treats each individual grain of the granular material as a rigid body, is the approach of choice for the numerical simulation of granular dynamics problems [7–12]. However, since DEM has to solve the dynamic equations of motion for each grain, a fully resolved simulation of a practical granular dynamics problem will lead to large degree of freedom (DOF) counts, which translates into high computational costs and large memory footprints. Moreover, in the majority of real-world problems the shape of the grains is nontrivial and poses additional challenges in formulating adequate frictional contact models and carrying out collision detection.

Recently, several inroads have been made toward representing discrete granular material via continuum representations. This opens the door to using simulation to tackle new classes



of problems that were intractable when approached in a fully resolved fashion via DEM. In a continuum-based approach the key is finding a relationship between the stress and the strain/strain-rate fields, i.e., a constitutive law, that will lead to a continuum model whose dynamics mimics well that of the granular material. Should a good constitutive law be identified, a smaller DOF count would be required to capture the dynamics of the deformable terrain. Several methods would then be available to discretize the continuum material. One class of methods is grid-based, or Eulerian, e.g., the finite element method (FEM) [13, 14]. Another class of approaches is particle-based, or Lagrangian, e.g., smoothed particle hydrodynamics (SPH) [15] and material point method (MPM) [16, 17].

An FEM solution can capture the behavior of a granular material in its flow, yet the computational cost is high due to inherently large deformations of the mesh. Without frequent remeshing, ill-shaped FEM elements can lead to low-accuracy solutions when the granular material is subject to plastic flow. SPH and MPM can avoid the disadvantages of the meshbased solution and were proved to be effective in simulating granular material problems with large deformation. In MPM the domain is projected against a *fixed* background grid [18]. The dynamics equations are solved on the background grid, whereas the state information (e.g., position, velocity) is stored and advected with the particles [19, 20]. MPM does not experience any of the drawbacks of ill-shaped elements since the background grid is fixed and experiences no deformation whatsoever. Compared with MPM, the SPH method is a pure Lagrangian particle-based solution that uses no background grid [21, 22]. The state information is advected with the SPH particles, and the dynamics equations are enforced at the location of the SPH particles instead of the nodes of the background grid, as is the case in MPM. The particles move based on the interactions among neighbor particles and the external forces, e.g., gravity. SPH method has proved very efficient in modeling and simulating of granular material problems with large deformation [23–26].

In this work, we use a two-way coupling algorithm discussed in [27], in which both large deformation of the granular material terrain and large overall motion of the solid bodies in three-dimensional space can be captured. In [27] the granular flow is modeled as an SPH-resolved continuum problem. The interaction between solid bodies and the granular material is posed and solved as a fluid-solid interaction (FSI) problem using so-called boundary conditions enforcing (BCE) particles [28, 29] attached to the boundary of the solid bodies. This coupling approach was already successfully applied to capture the interaction between a rigid/flexible multibody system and fluids in previous work [29–32]. To represent the dynamics of dense granular material and update the stress field, we employ a constitutive law, first proposed and used in the material point method (MPM) [33], and apply it in the context of the SPH method.

This contribution is organized as follows. Section 2 describes the two-way coupling, cosimulation approach for modeling granular material flows and its interaction with a multibody system via the SPH method. In Sects. 3 and 4, we describe a Curiosity Mars rover model, report on single-wheel test results and carry out mobility simulations for the Curiosity rover in hill climbing over granular terrains. The interest is in whether a suitably chosen traction control policy can improve rover battery drain. Various rover mobility scenarios are investigated to assess the robustness of the simulation solution. Section 5 summarizes concluding remarks and directions of future work.



# 2 Modeling approach

#### 2.1 Governing equations of deformable terrain: a continuum representation

In this work, a continuum representation is used in lieu of a discrete, granular material-based one when modeling deformable terrain in terramechanics applications. For the continuum, the field velocity vector  $\mathbf{u}$  and stress tensor  $\boldsymbol{\sigma}$  enter the momentum balance and continuity equations as [34]

$$\begin{cases} \frac{d\mathbf{u}}{dt} = \frac{\nabla \sigma}{\rho} + \mathbf{f}_b \\ \frac{d\rho}{dt} = -\rho \nabla \cdot \mathbf{u} \end{cases}$$
 for  $\mathbf{x} \in \Omega_f$ , (1)

where  $\Omega_f$  is the simulation domain occupied by the granular material,  $\rho$  is the bulk density of the deformable terrain, and  $\mathbf{f}_b$  represents the external force, e.g., gravitational pull. The total stress tensor  $\boldsymbol{\sigma}$  in the continuum is expressed as

$$\boldsymbol{\sigma} = \begin{bmatrix} \sigma_{xx} & \sigma_{xy} & \sigma_{xz} \\ \sigma_{xy} & \sigma_{yy} & \sigma_{yz} \\ \sigma_{xz} & \sigma_{yz} & \sigma_{zz} \end{bmatrix} = -p\mathbf{I} + \boldsymbol{\tau} , \qquad (2)$$

where  $\tau$  is the deviatoric component of the total stress tensor, and p is the isotropic pressure related to the trace of the tensor  $\sigma$ , i.e.,  $p = -\frac{1}{3} \text{tr}(\sigma) = -\frac{1}{3} (\sigma_{xx} + \sigma_{yy} + \sigma_{zz})$ . To track the history of the total stress tensor, a stress rate tensor should come into play. To this end, according to Hooke's law, a linear elastic relation between the Jaumann stress rate tensor and elastic strain tensors [33, 35–37] can be used to obtain the total stress rate tensor as

$$\frac{d\sigma}{dt} = \dot{\phi} \cdot \sigma - \sigma \cdot \dot{\phi} + 2G(\dot{\epsilon} - \frac{1}{3} \text{tr}(\dot{\epsilon})\mathbf{I}) + \frac{1}{3} K \text{tr}(\dot{\epsilon})\mathbf{I} \quad \text{for } \mathbf{x} \in \Omega_f ,$$
 (3)

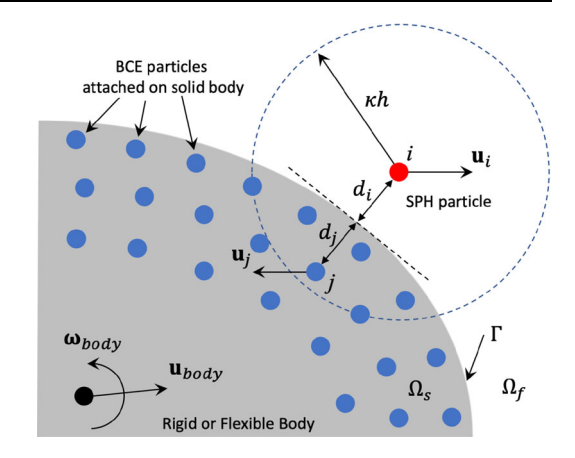
where the elastic strain rate tensor of the continuum is defined as  $\dot{\boldsymbol{e}} = \frac{1}{2} [\nabla \mathbf{u} + (\nabla \mathbf{u})^{\mathsf{T}}]$  when the material is not subject to plastic flow, the rotation rate tensor is expressed as  $\dot{\boldsymbol{\phi}} = \frac{1}{2} [\nabla \mathbf{u} - (\nabla \mathbf{u})^{\mathsf{T}}]$ , and G and K denote the shear and bulk moduli, respectively. Note that the expression of the elastic strain rate tensor given above only works in cases without a plastic flow. Once a plastic flow occurs in the granular material, the definition of the elastic strain rate tensor is slightly different. Details on handling the plastic granular material flow are available in [27].

# 2.2 Spatial discretization

The SPH method is used to discretize the momentum and continuity equations expressed in Eq. (1) and the total stress rate tensor relation in Eq. (3). In the SPH method the simulation domain (including the deformable granular material terrain, solid bodies, and wall boundary) is discretized via classic SPH particles and boundary conditions enforcing (BCE) particles, as shown in Fig. 1. The SPH particles are used to capture the dynamics of deformable granular material terrain; the BCE particles are used in conjunction with solid bodies or wall boundaries  $\Omega_s$  to enforce, in a co-simulation mode, the two-way coupling between the continuum and solid bodies in the multibody dynamics model. The motion of the SPH particles is obtained by solving Eqs. (1) and (3). However, the motion of the BCE particles is kinematically driven in this cosimulation framework and is subject to the motion of the solid bodies or wall boundary to which they are attached.



Fig. 1 SPH particles and BCE particles close to the solid body or wall boundary. The Dirichlet boundary condition is imposed by extrapolating the velocities to the BCE particles



According to the SPH method, the value of a function f at the position of particle i can be approximated as [38]

$$f_i = \sum_j f_j W_{ij} \mathcal{V}_j \,, \tag{4}$$

where  $V_i$  is the volume of particle i defined as  $V_i = (\sum_j W_{ij})^{-1}$ . Thus the mass associated with particle i can be obtained as  $m_i = \rho_i V_i$ . In Eq. (4),  $W_{ij}$  is the kernel function, which depends on the relative position of two neighbor particles in the support domain. In this work, we use a cubic spline function expressed as

$$W_{ij} = W(\mathbf{r}_{ij}) = \alpha_d \begin{cases} \frac{2}{3} - R^2 + \frac{1}{2}R^3, & 0 \le R < 1, \\ \frac{1}{6}(2 - R)^3, & 1 \le R < 2, \\ 0, & R \ge 2, \end{cases}$$
 (5)

where the relative position between particles i and j is defined as  $\mathbf{r}_{ij} = \mathbf{x}_i - \mathbf{x}_j$  with  $\mathbf{x}_i$  being the position of particle i,  $\alpha_d$  is a constant, which assumes the value  $3/(2\pi h^3)$  for a three-dimensional (3D) simulation, and the scaled length parameter R is defined as  $R = \frac{r_{ij}}{h}$  with h denoting the kernel length (one to two times of the initial particle spacing  $\Delta x$ ). With the kernel function  $W_{ij}$ , a field value, e.g., the velocity  $\mathbf{u}$  or density  $\rho$ , at the position of a neighbor particle j, when  $j \in \mathcal{N}_{h,i} = \{k : r_{ik} < 2h\}$ , contributes to the sum in Eq. (4) for approximating the function value at position i. Since the SPH particles advect with the granular material flow, it is necessary to update the list  $\mathcal{N}_{h,i}$  of neighbor particles of particle i.

For the gradient operator of a function f at the position of SPH particle i, both consistent and inconsistent discretizations are available [39]. The former, which gives more accurate results at a modest increase in computational effort [39–43], is the one embraced herein:

$$\nabla f_i = \sum_j (f_j - f_i) \left( \mathbf{G}_i \cdot \nabla_i W_{ij} \right) \mathcal{V}_j , \qquad (6)$$



where the gradient of the kernel function  $W_{ij}$  with respect to the position of particle i is expressed as

$$\nabla_{i} W_{ij} = \alpha_{d} \frac{1}{h} \frac{\mathbf{r}_{ij}}{r_{ij}} \begin{cases} -2R + \frac{3}{2}R^{2}, & 0 \le R < 1, \\ -\frac{1}{2}(2-R)^{2}, & 1 \le R < 2, \\ 0, & R \ge 2, \end{cases}$$
 (7)

and the matrix  $\mathbf{G}_i \in \mathbb{R}^{3\times 3}$  is a symmetric correction matrix for the gradient operator of particle i,  $\mathbf{G}_i \equiv -\left[\sum_j \mathbf{g}_{ij} \otimes \mathbf{r}_{ij}\right]^{-1}$ , with  $\mathbf{g}_{ij} \equiv \nabla_i W_{ij} \mathcal{V}_j$ ; see [39, 44]. Involving the correction matrix  $\mathbf{G}_i$  in the discretization of the gradient ensures an exact gradient for any linear function regardless of the  $h/\Delta x$  ratio [39]. This allows us to use a relatively smaller kernel length h in the simulation thereby reducing computational costs. Hence the consistent discretizations of the momentum balance and continuity equations are obtained by substituting Eq. (1) into Eq. (6), which yields

$$\frac{d\mathbf{u}_i}{dt} = \frac{1}{\rho_i} \sum_j (\boldsymbol{\sigma}_j - \boldsymbol{\sigma}_i) \cdot \mathbf{b}_{ij} + \mathbf{f}_{b,i} , \qquad (8)$$

$$\frac{\mathrm{d}\rho_i}{\mathrm{d}t} = -\rho_i \sum_j (\mathbf{u}_j - \mathbf{u}_i) \cdot \mathbf{b}_{ij} . \tag{9}$$

Similarly, the consistent discretization of the rotation rate and strain rate tensors assume the expression

$$\dot{\boldsymbol{\phi}}_{i} = \frac{1}{2} \sum_{i} \left[ \mathbf{u}_{ji} \mathbf{b}_{ij}^{\mathsf{T}} - \left( \mathbf{u}_{ji} \mathbf{b}_{ij}^{\mathsf{T}} \right)^{\mathsf{T}} \right], \tag{10}$$

$$\dot{\boldsymbol{\varepsilon}}_{i} = \frac{1}{2} \sum_{i} \left[ \mathbf{u}_{ji} \mathbf{b}_{ij}^{\mathsf{T}} + \left( \mathbf{u}_{ji} \mathbf{b}_{ij}^{\mathsf{T}} \right)^{\mathsf{T}} \right], \tag{11}$$

where  $\mathbf{b}_{ij} \equiv \mathbf{G}_i \cdot \nabla_i W_{ij} \mathcal{V}_j$ . Finally, the consistent discretization of the total stress rate tensor is obtained by substituting Eqs. (10) and (11) into Eq. (3), which yields

$$\frac{d\sigma_{i}}{dt} = \frac{1}{2} \left\{ \sum_{j} \left[ \mathbf{u}_{ji} \mathbf{b}_{ij}^{\mathsf{T}} - \left( \mathbf{u}_{ji} \mathbf{b}_{ij}^{\mathsf{T}} \right)^{\mathsf{T}} \right] \sigma_{i} - \sigma_{i} \sum_{j} \left[ \mathbf{u}_{ji} \mathbf{b}_{ij}^{\mathsf{T}} - \left( \mathbf{u}_{ji} \mathbf{b}_{ij}^{\mathsf{T}} \right)^{\mathsf{T}} \right] \right\} 
+ G \left\{ \sum_{j} \left[ \mathbf{u}_{ji} \mathbf{b}_{ij}^{\mathsf{T}} + \left( \mathbf{u}_{ji} \mathbf{b}_{ij}^{\mathsf{T}} \right)^{\mathsf{T}} \right] - \frac{1}{3} \text{tr} \left( \sum_{j} \left[ \mathbf{u}_{ji} \mathbf{b}_{ij}^{\mathsf{T}} + \left( \mathbf{u}_{ji} \mathbf{b}_{ij}^{\mathsf{T}} \right)^{\mathsf{T}} \right] \right) \mathbf{I} \right\} 
+ \frac{1}{6} K \left\{ \text{tr} \left( \sum_{j} \left[ \mathbf{u}_{ji} \mathbf{b}_{ij}^{\mathsf{T}} + \left( \mathbf{u}_{ji} \mathbf{b}_{ij}^{\mathsf{T}} \right)^{\mathsf{T}} \right] \right) \mathbf{I} \right\} .$$
(12)

## 2.3 Boundary conditions

In this work, we model a two-way coupling approach by imposing a Dirichlet (no-slip and no-penetration) boundary condition (BC) for the deformable granular material terrain at the



solid boundary (moving wheels or fixed wall). To accurately impose a Dirichlet BC for the granular material velocity, a full support domain contained in  $(\Omega_f \cup \Omega_s)$  should be attained to guarantee accurate SPH approximation for particles close to the boundary  $\Gamma$ . To this end, as shown in Fig. 1, we follow the strategy proposed in [41, 42, 45–47] to generate several layers of BCE particles in the solid area  $\Omega_s$  close to the boundary  $\Gamma$ . The velocities of the BCE particles can be linearly extrapolated from the SPH particle velocities close to the boundary, i.e.,

$$\mathbf{u}_j = \frac{d_j}{d_i} (\mathbf{u}_B - \mathbf{u}_i) + \mathbf{u}_B , \qquad (12)$$

where  $d_i$  and  $d_j$  represent the perpendicular distances to the solid boundary  $\Gamma$  for an SPH particle i and a BCE particle j, respectively. Here  $\mathbf{u}_B$  denotes the velocity at the solid boundary, which is expressed as

$$\mathbf{u}_B = \mathbf{u}_{body} + \boldsymbol{\omega}_{body} \times \mathbf{r}_c(\mathbf{x}) \quad \text{for } \mathbf{x} \in \Gamma, \tag{13}$$

where  $\mathbf{u}_{body}$  and  $\boldsymbol{\omega}_{body}$  are the translational and angular velocities of the solid body (e.g., the moving rover wheel), respectively, and  $\mathbf{r}_c(\mathbf{x})$  denotes the vector from the center of mass (e.g., the wheel center) of the solid body to the location  $\mathbf{x}$  at the boundary  $\Gamma$ . Note that the velocities of the BCE particles extrapolated from that of the SPH particles and the solid boundary are only used to enforce the Dirichlet BCs; these velocities cannot be used to advect the BCE particles since they will move along with the solid body to which they are rigidly attached.

For the total stress tensor  $\sigma_j$  at the position of a BCE particle j, we follow the approach in [48] to extrapolate it from the total stress tensor of the SPH particles close to the boundary  $\Gamma$ , i.e.,

$$\sigma_{j} = \frac{\sum_{i \in \Omega_{f}} \sigma_{i} W_{ji} + [diag(\mathbf{f}_{b} - \mathbf{f}_{j})] \sum_{i \in \Omega_{f}} \rho_{i} [diag(\mathbf{r}_{ji})] W_{ji}}{\sum_{i \in \Omega_{f}} W_{ji}},$$
(14)

where  $\mathbf{r}_{ji} = \mathbf{x}_j - \mathbf{x}_i$ , the function  $diag(\mathbf{f}_b - \mathbf{f}_j)$  creates a diagonal matrix from the vector  $\mathbf{f}_b - \mathbf{f}_j$ , and so does the function  $diag(\mathbf{r}_{ji})$ ,  $\mathbf{f}_b$  is the body force of the granular material (e.g., the gravity), and  $\mathbf{f}_j$  is the inertial force associated with the BCE particle j and can be evaluated as

$$\mathbf{f}_{i} = \dot{\mathbf{u}}_{\text{body}} + \dot{\boldsymbol{\omega}}_{\text{body}} \times \mathbf{r}_{ic} + \boldsymbol{\omega}_{\text{body}} \times (\boldsymbol{\omega}_{\text{body}} \times \mathbf{r}_{ic}) , \qquad (15)$$

where  $\mathbf{r}_{jc}$  is the vector from the solid body's center of mass to the position of the BCE particle j. The total force  $\mathbf{F}_{body}$  and torque  $\mathbf{T}_{body}$  exerted by the deformable terrain upon the solid body are then calculated by summing the forces contributed by the SPH particles onto the BCE particles as described in the conservative SPH method [49], i.e.,

$$\mathbf{F}_{\text{body}} = \sum_{j \in \Omega_{\delta}} m_j \, \dot{\mathbf{u}}_j \quad \text{and} \quad \mathbf{T}_{\text{body}} = \sum_{j \in \Omega_{\delta}} \mathbf{r}_{jc} \times (m_j \, \dot{\mathbf{u}}_j) \,. \tag{16}$$

#### 2.4 Update of field variables

In this work, we update the field variables (e.g., the velocity, position, and total stress tensor) of the SPH particles using an explicit predictor–corrector time integration scheme with



second-order accuracy [50, 51]. There are two half steps involved in this integration scheme for each time step. In the first half step, we first predict an intermediate value of velocity  $\bar{\mathbf{u}}_i$ , position  $\bar{\mathbf{x}}_i$ , and total stress tensor  $\bar{\sigma}_i$  at  $t + \frac{\Delta t}{2}$ . Using the predicted values, we evaluate again Eqs. (8), (12), and (17) to update the velocity, position, and total stress tensor to the corrected values. Finally, we update the field variables of the SPH particles based on the initial and corrected values at  $t + \Delta t$ . More details about the interaction scheme for granular material dynamics can be found in [27].

To enforce the condition that the particles advect at a velocity close to an average velocity of their neighboring particles, in this study, we use the so-called XSPH technique [50]. According to the XSPH method, the relationship between the displacement of the SPH particle *i* and its velocity is expressed as

$$\frac{\mathrm{d}\mathbf{x}_i}{\mathrm{d}t} = \mathbf{u}_i - \xi \sum_j \mathbf{u}_{ij} W_{ij} \mathcal{V}_j , \qquad (17)$$

where the second term is a correction term with the coefficient  $\xi$  in this work being set to 0.5. More details about the XSPH method used in granular material dynamics can be found in [27]. Therein a comprehensive study about how to choose the value of the coefficient  $\xi$  was performed by gauging the influence of  $\xi$  onto the kinetic energy of the dynamic system.

Since the advection of SPH particles with the granular material flow can lead to high particle disorder scenarios and hence a low computational accuracy after long-time simulation, we employ a particle shifting technique (PST) to provision against such scenarios in this study. The original form of the PST was proposed in [52] and has been applied in many SPH applications; see, for instance [40, 41, 52]. However, the original PST cannot be applied to problems with free surfaces since it requires a complete support domain for the SPH particles. Thus we employ a new penetration-based particle shifting technique (PPST) proposed in [27] which is stable, simple, and easy to implement. Most importantly, no tracking is required for SPH particles close to free surface. The shifting vector of the PPST scheme is expressed as

$$\Delta \mathbf{r}_{i} = \begin{cases} \beta_{1} \| \mathbf{u}_{i} \| \Delta t \sum_{j} \Delta r_{ij} \mathbf{e}_{ij}, & \Delta r_{ij} > 0, \\ \beta_{2} \| \mathbf{u}_{i} \| \Delta t \sum_{j} \Delta r_{ij} \mathbf{e}_{ij}, & \Delta r_{0} < \Delta r_{ij} \leq 0, \\ \beta_{2} \| \mathbf{u}_{i} \| \Delta t \sum_{j} \Delta r_{0} \mathbf{e}_{ij}, & \Delta r_{ij} \leq \Delta r_{0}, \end{cases}$$

$$(18)$$

where  $\mathbf{e}_{ij}$  is the unit vector from particle j to i, and based on recommendations made in [27], we chose  $\beta_1=3$  and  $\beta_2=1$ . The relative penetration depth between particle i and j is defined as  $\Delta r_{ij}=\frac{D_{s,i}-r_{ij}}{D_{s,i}}$ , where  $D_{s,i}=2\sqrt[3]{\frac{3m_i}{4\pi\rho_i}}$  is the diameter of the SPH particle. The critical value of the penetration depth is set to  $\Delta r_0=-0.1$  in this work.

To accurately update the value of the total stress tensor  $\sigma$  of the deformable granular material terrain, we employ an approach originally proposed in MPM [33] and apply it within the framework of SPH. The total stress tensor of all SPH particles is first updated explicitly from t to  $t + \Delta t$  according to the predictor-0corrector scheme described in [27, 50, 51]. Once the update is done, at the end of this time step, the total stress tensor is then further corrected based on a four-step postprocessing strategy: (i) Calculate the value of  $p^*$  and  $\tau^*$  according to the value of total stress tensor  $\sigma^*$ , which is already obtained through the predictor-corrector scheme using Eq. (2); (ii) If  $p^* < 0$ , then simply set  $\sigma = \mathbf{0}$  at  $t + \Delta t$  and start a new integration time step; (iii) If  $p^* > 0$ , then set  $p = p^*$ , compute the double inner



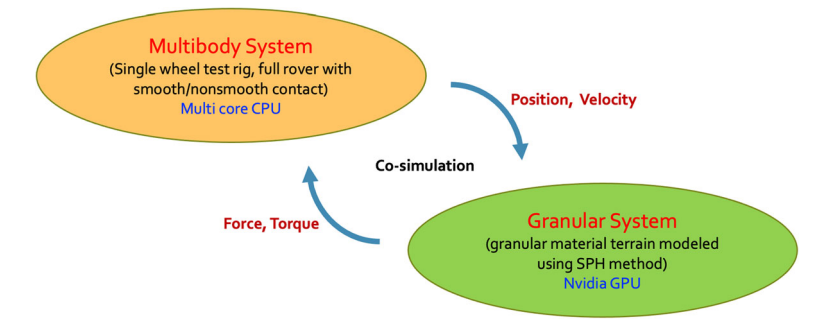


Fig. 2 The co-simulation setup in Chrono::FSI

product of  $\tau^*$  as  $\bar{\tau}^* = \sqrt{\frac{1}{2}(\tau_{\alpha\beta}^*) : (\tau_{\alpha\beta}^*)}$ , and compute  $S_0$  as  $S_0 = \mu_s p^*$ , where  $\alpha$  and  $\beta$  are indices for the stress components; (iv) If  $\bar{\tau}^* < S_0$ , then simply set  $\tau = \tau^*$  as the deviatoric component of  $\sigma$  at  $t + \Delta t$  since no plastic flow occurs at this moment; else, use the Drucker–Prager yield criterion to scale the deviatoric component of  $\sigma$  back to the yield surface as  $\tau = \frac{\mu p^*}{\bar{\tau}^*} \tau^*$ . Here the friction coefficient used in step (iii) is defined as  $\mu = \mu_s + \frac{\mu_2 - \mu_s}{I_0/I + 1}$  [33], where  $\mu_s$  is the static friction coefficient, and  $\mu_2$  is the limiting value of  $\mu$  as  $I \to \infty$ ;  $I_0$  is a material constant, which is set to 0.03 in this work; I is the inertial number. More details about the four-step strategy and the calculation of parameters can be found in [27].

# 2.5 Cosimulation setup

Two modules come into play in the cosimulation framework implemented in Chrono. One is the multibody dynamics simulation engine, which is used to propagate forward in time the motion of the solid bodies, e.g., the dynamics of the Curiosity rover. The frictional contact between the rigid bodies is handled therein using a differential variational inequality (DVI) approach [53, 54]. The second module handles the dynamics of the granular material; this is accomplished using the SPH methodology described in Sects. 2.2–2.4. Since the SPH particles used to discretize the simulation domain are larger than the terrain grain size, the degree of freedom count is significantly reduced in the continuum approach. The SPH simulation support is implemented in Chrono::FSI, which is a submodule of Chrono that uses GPU acceleration.

As mentioned in Sect. 2.3 and illustrated in Fig. 1, BCE particles are attached to the rigid bodies to account via Dirichlet BCs for the interaction between rigid bodies and deformable terrain. The cosimulation is anchored by a four-step procedure, illustrated in Fig. 2, to advance the simulation one time step at a time: (i) Run one dynamics step of the multibody system and update the position and velocity of each body in the system; (ii) Update the position and velocity of the BCE particles according to the rigid body to which they are attached and pass this information to the deformable terrain simulation module to enforce no-slip, no-penetration Dirichlet BCs; (iii) Run one dynamics step for the deformable terrain and update the position, velocity, and stress tensor for each SPH particle; (iv) Calculate the net force and torque acting upon each rigid body using the interaction between SPH particles and BCE particles and then pass these loads back to the multibody simulation module. The communication between the two modules can be done at each time step or every few time steps. Typically, the dynamics of the deformable terrain calls for a smaller step size.



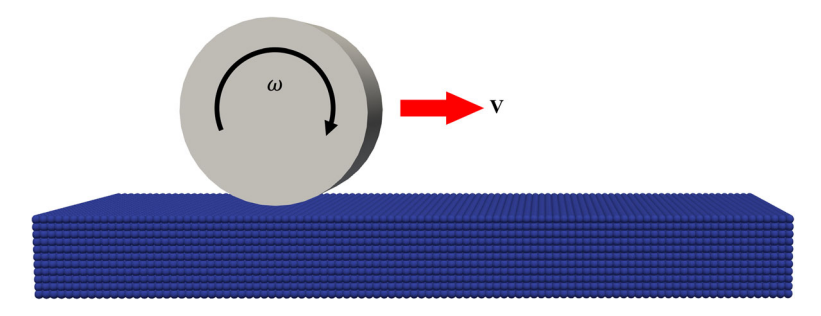


Fig. 3 Schematic of the setup for the single cylindrical wheel test

# 3 Single-wheel test

We report results for the single-wheel test, in which one wheel moves under controlled slip and normal loading conditions within a confined soil bin filled with granular material. The drawbar pull force, wheel torque, and wheel sinkage were measured for three different wheels operating at several slip ratios. To produce and maintain a desired slip ratio, the wheel was rolled onto the granular material terrain with a constant angular velocity  $\omega$  and at the same time translated with a constant, suitably chosen horizontal velocity v. The resulting value was slip =  $1 - \frac{v}{\omega r_w}$ , where  $r_w$  is the radius of the wheel. For the methodology proposed, this test is regarded as a validation stepping stone toward system-level simulation of a full rover. Unfortunately, there is limited amount of experimental data that this exercise could draw on.

## 3.1 Cylindrical wheel

The cylindrical wheel had a width of w = 0.16 m and a radius of  $r_w = 0.13$  m. The angular velocity was fixed as 0.3 rad/s. The numerical tests in Chrono::FSI were conducted by simulating a soil containing 60,000 SPH particles. In this case, both the initial particle spacing and the smoothing length are set to 0.01 m. The wheel was placed right above the soil bin and rolled at the desired slip ratio for 20 s; see Fig. 3 for the simulation setup. The density and frictional coefficient of the soil were 1700 kg/m<sup>3</sup> and 0.7. The Young modulus and Poisson ratio of the granular material were set to  $1 \times 10^6$  Pa and 0.3, respectively. The normal load on the wheel was 130 N. This includes the weight of the wheel and testing rig - a combined mass of 13.25 kg factored in under earth gravitational pull. Figure 4 shows results for the drawbar pull force, wheel torque, and wheel sinkage, respectively. As the slip ratio of the wheel increases, the drawbar pull force and torque also increase. However, the sinkage shows the minimum value when the slip ratio is close to zero. The results were compared against experiment data reported in [55]; the force, torque, and sinkage all show good agreement. Figure 5 illustrates the SPH particle distribution of the terrain and the position of the cylindrical wheel. The screenshots were captured when t = 15 s with slip ratio being set as -0.5, 0, and 0.5, respectively.

#### 3.2 Toroidal tire

The rigid toroidal tire had a width of w = 0.2 m and a radius of  $r_w = 0.305$  m. The angular velocity was fixed as 0.175 rad/s. The numerical tests in Chrono were conducted by simulating a soil bin via 1,800,000 SPH particles. In this case, both the initial particle spacing



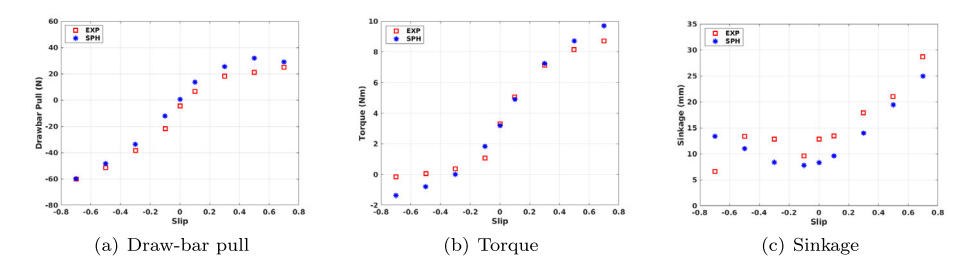


Fig. 4 Drawbar pull force, torque, and sinkage of the wheel vs. slip ratio curves for a normal load of 130 N. Data label EXP is experimental data according to [55]. SPH data are obtained using simulation

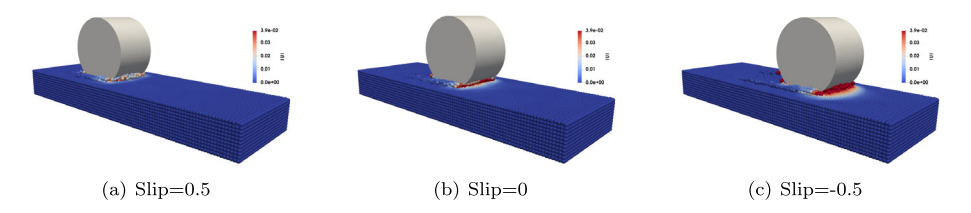


Fig. 5 SPH particle distribution at t = 15 s with different slip ratios with colors corresponding to the magnitude of velocity (m/s) (Color figure online)

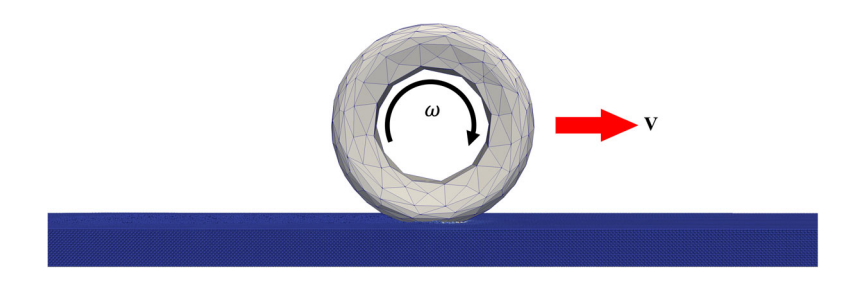


Fig. 6 Skeleton of the single toroidal rubber tire test setup

and the smoothing length were set as 0.005 m. The tire was placed right above the soil bin and rolled at the desired slip ratio for 50 s; see Fig. 6. The density and frictional coefficient of the soil were  $1700 \text{ kg/m}^3$  and 0.9. The Young modulus and Poisson ratio of the granular material were set to  $1 \times 10^6$  Pa and 0.3, respectively. The normal load on the wheel was as produced by a mass of 105.22 kg under earth gravitational pull. Figure 7 reports drawbar pull force, wheel torque, and wheel sinkage. The results show that as the slip ratio increases, the drawbar pull force and torque also increase. However, the drawbar pull drops slightly when slip ratio is large. The sinkage decreases with a negative value and increases with a positive value. A minimum value can be observed when the slip ratio is close to zero. Figure 8 shows the SPH particle distribution of the terrain and the position of the meshed tire. The screenshots were captured when t = 40 s with slip ratios of -0.5, 0, and 0.5, respectively.

#### 3.3 Wheel with grousers

The rigid wheel with grousers had a width of w = 0.25 m and a radius of  $r_w = 0.28$  m; the thickness of the grousers was 10 mm. The angular velocity was fixed as 0.192 rad/s. The



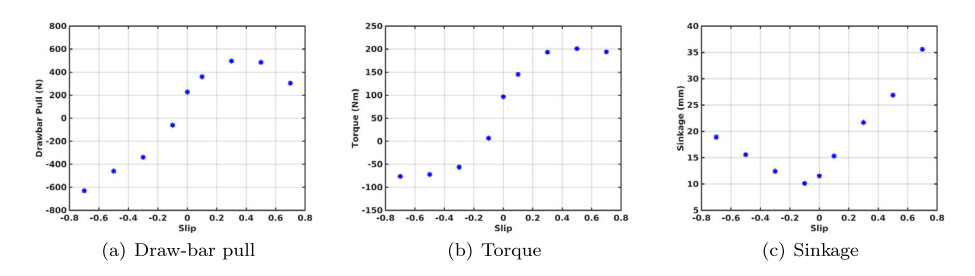


Fig. 7 Toroidal rubber tire: drawbar pull force, torque, and sinkage of the tire vs. slip ratio curves for a normal load associated under earth gravitational pull with a mass of 105.22 kg

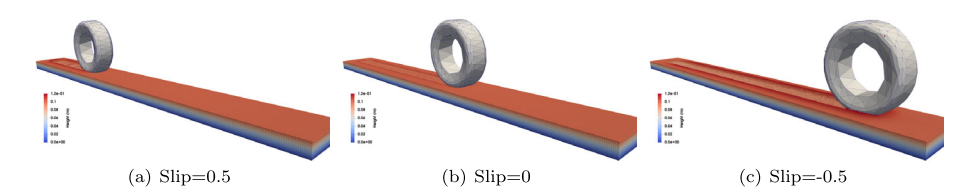


Fig. 8 Toroidal tire: SPH particle distribution at t = 40 s with different slip ratios with colors corresponding to the height of the particle (m). The tire is represented with mesh (Color figure online)

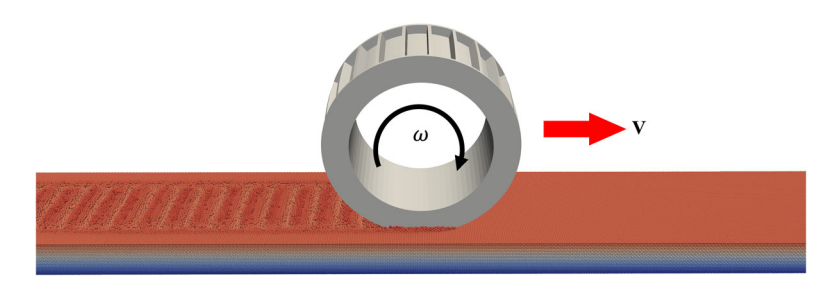
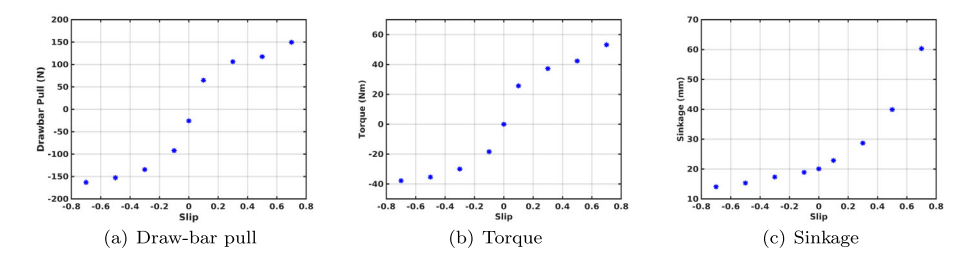


Fig. 9 Skeleton of the single wheel with grousers (Color figure online)

numerical tests in Chrono::FSI were conducted by simulating a soil bin via 1,700,000 SPH particles. In this case, both the initial particle spacing and the smoothing length are set as 0.005 m. The rigid wheel was placed right above the soil bin and rolled at the desired slip ratio for 50 s; see Fig. 9. The density and frictional coefficient of the soil were  $1700 \text{ kg/m}^3$  and 0.9. The Young modulus and Poisson ratio of the granular material were set to  $1 \times 10^6 \text{ Pa}$  and 0.3, respectively. The normal load on the wheel was as produced by a mass of 17.5 kg under earth gravitational pull. Figure 10 shows the drawbar pull force, wheel torque, and wheel sinkage. As the slip ratio increases, the drawbar pull force, torque, and sinkage also increase. The sinkage for the wheel with grousers is vastly different from the sinkage for the wheel without grousers (see Figs. 4(c) and 7(c)). Figure 11 displays the SPH particle distribution of the terrain and the meshed rigid wheel. The screenshots were captured when t = 30 s, for slip ratios -0.5, 0, and 0.5. The wheel footprint observed in the screenshots correlates with the position of the wheel grousers.

Compared to a DEM-based solution, the number of degrees of freedom can be significantly reduced by employing the outlined SPH-enabled continuum representation. For small degree of freedom counts, we hope to use SPH particles that are as large as possi-





**Fig. 10** Wheel with grousers: Drawbar pull force, torque, and sinkage of the wheel vs. slip ratio curves. Load as produced by 17.5 kg under earth gravitational pull

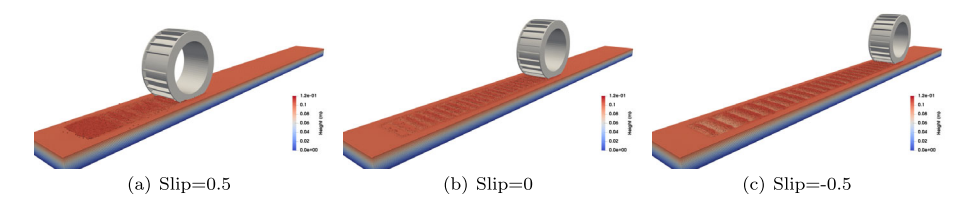


Fig. 11 Wheel with grousers: SPH particle distribution at t = 30 s with different slip ratios with colors corresponding to the height of the particle (unit: m) (Color figure online)

ble. However, to capture the interaction between soil and a wheel that has small features (e.g., fine grousers), we have to use small BCE particles to capture the two-way coupling between the rover and terrain. Since the implementation only supports a single resolution spatial discretization, the SPH particles used to discretize the terrain soil are correspondingly small. The computational cost for a single wheel is not a matter of great concern since the patch of terrain is relatively small. However, in the full rover simulation with larger swaths of terrain (flat-uphill-flat terrain in the following section), the computational cost can become prohibitive. Against this backdrop, simulations were performed to understand how the grouser thickness influences the drawbar pull force, torque, and sinkage. The thickness of the grousers varied from 4 mm to 12 mm. The spacing between SPH particles was identical to the grouser thickness. The diameter of BCE particles used to represent the wheel mesh geometry was also equal to the grouser thickness. The purpose of this test is motivated as follows: we would like to use large size particles so that we finish simulation fast – large particles means fewer particles to cover a patch of terrain. For instance, when using SPH particles of 12 mm instead of 3 mm, in theory, the 3D simulation would run approximately 64 times faster; this is a rough rule of thumb, since other factors come into play. The question is how are results going to change if slightly larger grousers and larger particles are used? The results of this inquiry are presented below, and the short answer is that increasing the particle/grouser size up to a point does not change qualitatively and quantitatively the results too much. Note that the conclusions drawn here hold for the specific wheel with the specific number of grousers used in this work. Other terrain types and wheel geometries would require similar analysis to gain insights that allow for a reduction of the computational burden associated with the problem of interest.

Figures 12, 13, and 14 show the time histories of the drawbar pull force, wheel torque, and wheel sinkage with different slip ratios and different grouser thicknesses. The results indicate that as the slip ratio increases, the drawbar pull force, torque, and sinkage also increase. Note that the drawbar pull force, wheel torque, and wheel sinkage did not show



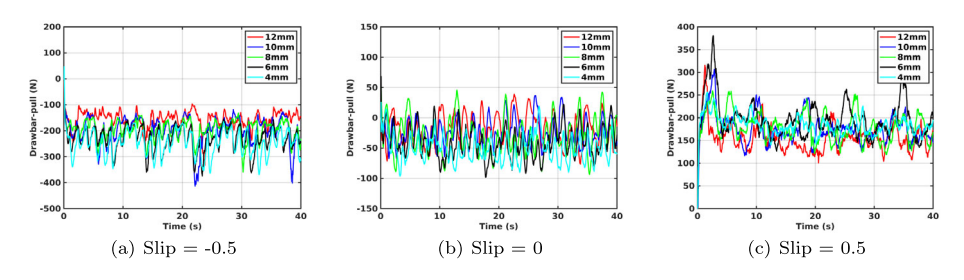


Fig. 12 Wheel with grousers: Drawbar pull force vs. time curves. Particle size is identical to the grouser thickness (Color figure online)

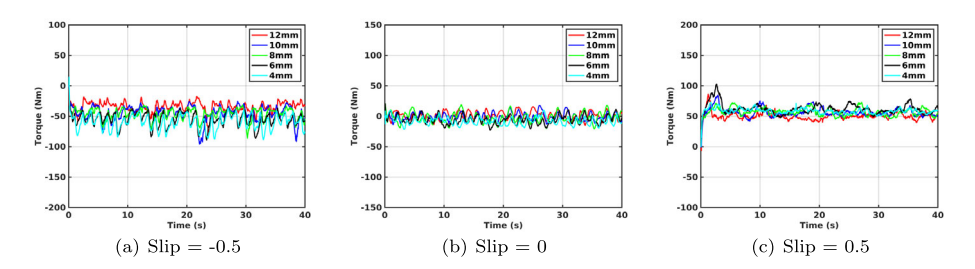


Fig. 13 Wheel with grousers: Wheel torque vs. time curves. Particle size is identical to the grouser thickness (Color figure online)

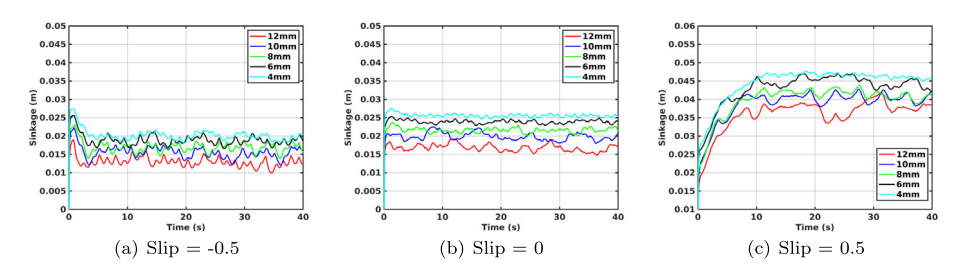
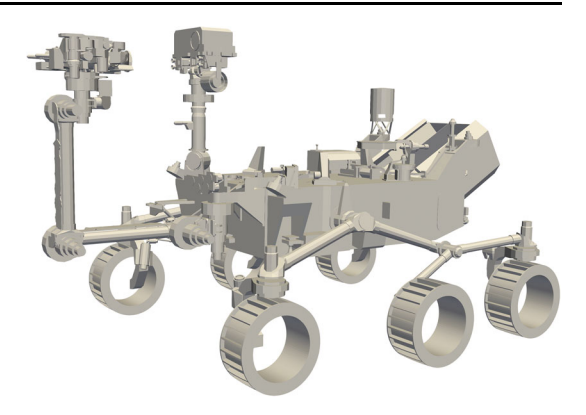


Fig. 14 Wheel with grousers: Wheel sinkage vs. time curves. Particle size is identical to the grouser thickness (Color figure online)

significant differences when the grouser thickness changed from 4 mm to 12 mm. However, the number of particles can be significantly reduced, from about 3,000,000 to 150,000. As a result, the real time factor can be reduced from 1440:1 to 120:1, i.e., it takes 120 seconds to simulate one second of physics, instead of 1440 seconds. This experiment also suggests that the accuracy of the 12 mm or 10 mm simulations is good enough to capture the physics of interest for the single-wheel test. This observation will allow us to make the full rover simulations faster in the following section. Indeed, running full rover simulation with small grouser thickness on the wheel is taxing owing to a large number of SPH and BCE particles. Yet the results in this subsection suggest that going to large grouser size, at least early on in the control policy design for rover mobility, is a reasonable decision to make.



Fig. 15 Curiosity Mars rover model with 10-mm grouser wheels



#### 4 Full rover simulation

## 4.1 The Curiosity Mars rover model

Figure 15 shows the Curiosity model used in the full rover simulation. The rover was driven by prescribing angular velocity values to its wheels; these six angular velocities need not all be the same. As elaborated upon in the previous subsection, the wheel grousers were 10 mm thick. The rover chassis had an approximate length of 3.94 m, width of 1.56 m, and a height of 1.58 m. The total mass of the rover model was approximately 899 kg. The suspension prevents the rover from uncontrolled yaw and body motion. For improved traction and rover stability, the suspension design also prevents both sides of the rover wheels being lifted up when one side of the rover hits an obstacle. The geometry information is available on NASA public website [56].

The two front suspension arms were connected to the rover body through a revolute joint. The two rear suspension arms were connected to the two front suspension arms through a revolute joint. All six wheels had been connected to the suspension arms through a revolute joint at the center of the wheel. The rover body and the wheels had nontrivial 3D shapes, both defined by triangular meshes. To handle the wheel-terrain interaction, BCE particles were attached onto the wheels using the triangular meshes that define the rigid body. To generate the BCE particles for a nontrivial 3D geometry defined with mesh, we used a mesh-to-point cloud conversion tool [57]. Figure 16 shows the original mesh of the wheel and its particle representation generated via spherical decomposition. The radius, width of the wheel, and number of grousers were identical to those on the actual Curiosity wheel. The friction and contact between solid bodies were handled via DVI as previously indicated.

Several simulations were performed to assess rover simulation robustness for operation in an flat-uphill-flat mobility scenario. The granular material-liked soil was only stored on the surface of the flat-uphill-flat terrain with a thickness of 0.1 m, as shown in Fig. 17. The length L of the lower flat and upper flat terrain was fixed to 3 m. The length L of the uphill terrain in the x direction was also fixed to 3 m, whereas the height H was changed from 1 m to 2 m. Thus the corresponding angles of the uphill terrain varied from 18° to 34°. The friction coefficient of the granular material was changed from 0.6 to 0.9. The six-wheel rover was placed right in front of the incline on the flat terrain. Once started, the rover moved with a fixed/varying angular velocity at each wheel. The Young modulus, density, and Poisson ratio of the granular material were set to  $1 \times 10^6$  Pa,  $1700 \text{ kg/m}^3$ , and 0.3, respectively. The simulations were performed under the Mars gravitational pull  $3.721 \text{ m/s}^2$ . The average



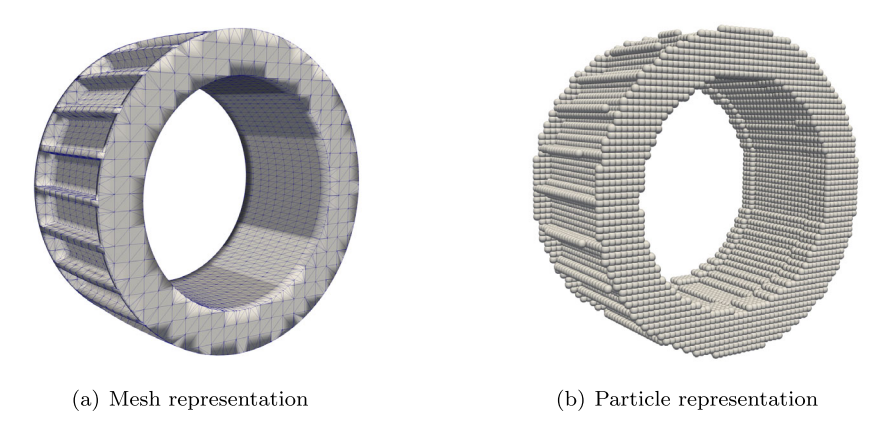


Fig. 16 Mesh and particle representation of the rover wheel with 10-mm grousers

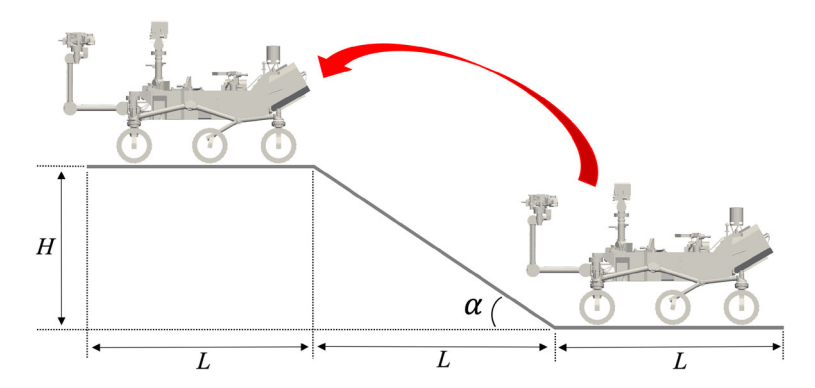


Fig. 17 Simulation setup of the flat-uphill-flat terrain

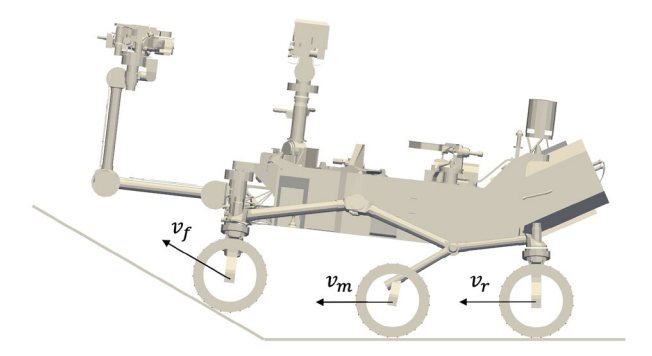
diameter of the soil particles used in this simulation is 0.001 m, whereas the size of the SPH particles was set as 0.01 m. The total number of SPH particles used to model this problem was 5,300,000. For a 10-s simulation, the total computational cost is about 3.5 hours on an Nvidia A100 GPU card. The integration step size was 2.5e-4 s.

### 4.2 Traction control strategy

Originally launched without traction control, Curiosity experienced intense wear and tear [58], which required a firmware update that came several years after its launch while it was in operation [59]. This experience underlined the importance of a traction control policy, which in this contribution is derived in the presence of deformable terrain. In the scenario considered, the rover moved from the lower flat terrain to the upper flat terrain (shown in Fig. 17). A simple traction control algorithm was implemented with an eye toward reducing energy. A "control on" scenario, which varied the angular velocity at each wheel as the rover climbed, was compared against the "control off" scenario, in which all wheels had constant and equal angular velocities. Figure 18 shows the side view of the Curiosity rover model with two front wheels touching on the incline. With this picture in mind, assume that no traction control algorithm is used, i.e., all six wheels rotate with constant angular velocity. When all



Fig. 18 Side view of the Curiosity rover model with the front wheel touching on the incline



the six wheels are on the flat terrain or all of them are on the incline, things are working well. However, when the front wheels start to move on the incline and the middle and rear sets of wheels are still on the lower flat terrain, since the front wheels have to move faster than the middle and rear wheels  $(v_f > v_m = v_r)$ , they will start to produce negative slip. For a similar reason, when the front wheels leave the incline and rotate on the upper flat terrain, since the front wheels have to move slower than the middle and rear wheels  $(v_f < v_m = v_r)$ , they will experience positive slip. As a rule of thumb, for preserving the battery, neither positive nor negative slips are desirable since a nonzero slip will make the wheel shear the ground or bulldoze the terrain, and a more powerful motor is usually required accommodate such a scenarios, as it can be observed from Fig. 13.

To avoid the issue described above and increase the efficiency of the rover climb, a simple traction control algorithm was used to adaptively change the angular velocity assigned to each set of wheels. Assume that the constant angular velocity used in the "control off" simulation was  $\omega_{\rm off}$ . We also defined a base angular velocity in the "control on" simulation as  $\omega_{\rm on}$ , which is equal to  $\omega_{\rm off}$ . Then, the algorithm if formulated as the following five-step control policy:

STEP 1: Read the translational velocity at the center of each wheel at the end of the current time step, i.e.,  $v_f$ ,  $v_m$ , and  $v_r$  shown in Fig. 18;

STEP 2: Find the maximum translational velocity among the six wheels, which is defined as  $v_{\text{max}}$ ;

STEP 3: Calculate the rescale ratio of the angular velocity that will be requested from the motor on each wheel for the next time step, i.e.,  $\mathbb{R} = \frac{v}{v_{\text{max}}}$ ;

STEP 4: Calculate the angular velocity for each motor on each wheel  $\omega = \omega_{\rm on} \mathbb{R}$ ;

STEP 5: Set the new angular velocity  $\omega$  for each motor and take one time step.

Note that in simulation, this is simple; in practice, implementing this policy may be nontrivial owing to sensing limitations. The control policy was executed every timestep. Nonetheless, since the purpose here is to test the rover and terrain, the issue of how to obtain this information is eschewed.

#### 4.3 Mobility simulation on a flat-uphill-flat terrain

We performed two groups of simulations – with "control on", and "control off", the latter using a constant angular velocity  $\omega_{off}$ ). Figure 19 shows the time histories of the wheel slip, torque, and power requirement for the traction control on and off simulations. The friction coefficient was set to 0.9; the height of the incline was 1 m. The left two sub-figures indicate that the wheel slip was well controlled in the simulation with the traction control algorithm. The vehicle experiences identical slips at each of its six wheels. The slip is much closer to



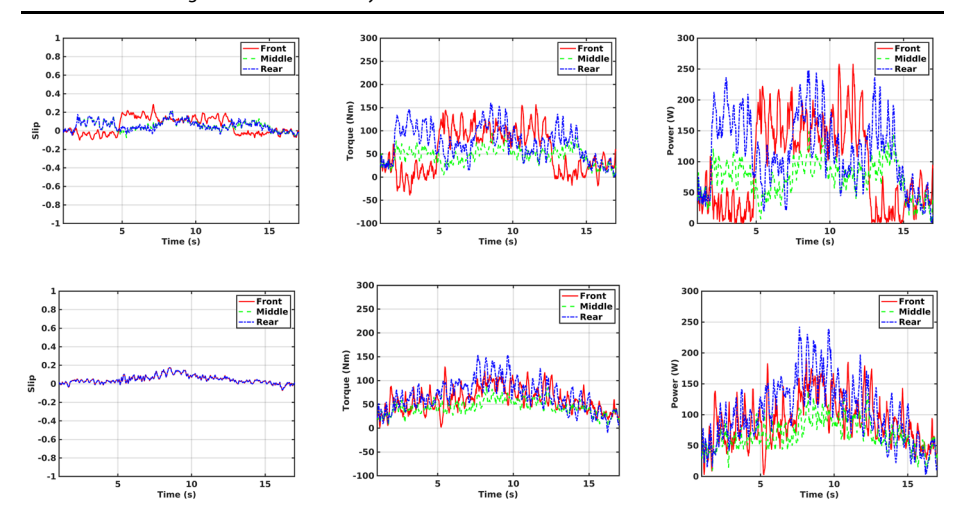


**Fig. 19** Wheel slip, torque, power vs. time curves. Friction coefficient is 0.9. Height of the uphill terrain is 1 m. The upper three plots correspond to the traction "control off" scenario; the lower three corresponds to the traction "control on" case

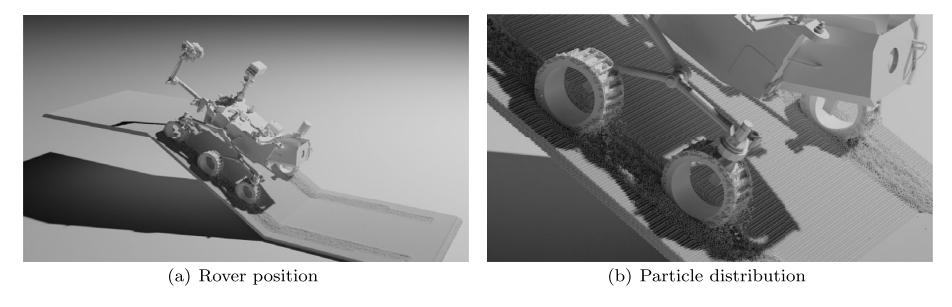
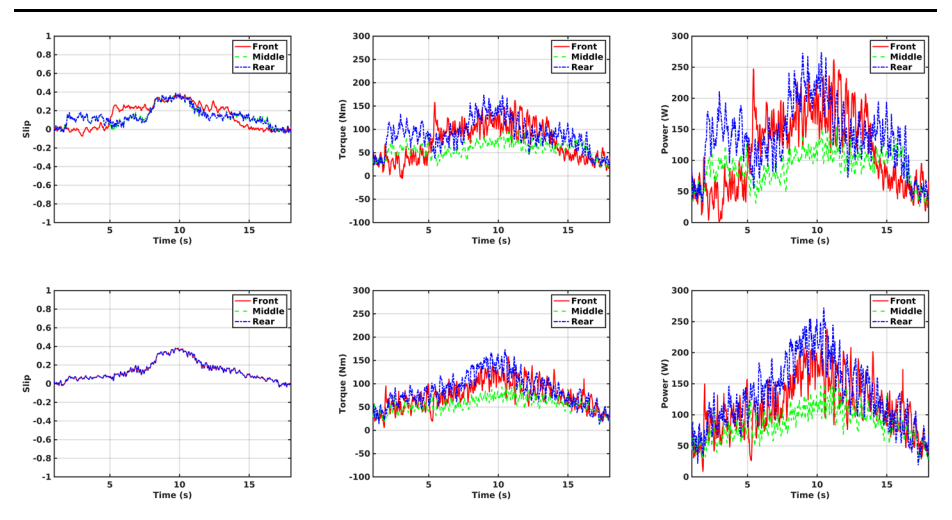


Fig. 20 Rover position on the uphill terrain and the local particle distribution at t = 15 s. The terrain height was 2 m; the friction coefficient was 0.9

zero especially at the beginning of the simulation (first 5 seconds), when the front wheel was already on the incline and the middle and rear wheels were still on the lower flat terrain. The other four sub-figures indicate that the peak torque and power are smaller after turning on the control policy. Both the torque and power of each wheel are closer to each other when the wheels were not on the same terrain. This is a marked improvement as there is balance among all wheels; i.e., we avoided a situation in which some of the wheels pushed the rover really hard, while other wheels were almost idle. We also measured the total energy usage for the rover as it moved from the lower flat terrain to the upper flat terrain, see Fig. 17. The traction control algorithm led to 8% energy savings. Considering that the algorithm doesn't help to save energy when all wheels are on the incline/flat terrain at the same time, we also did a more focused measurement—from the moment the front wheels started to move on the incline to the moment the rear wheels left the lower flat terrain. This was the stage when the traction control algorithm contributed most. During this stage, the "control on" policy led to 18% energy savings.

Finally, to assess the sensitivity and robustness of the rover simulation, we tested various scenarios with different friction coefficients and uphill slopes. A snapshot of one of these





**Fig. 21** Wheel slip, torque, power vs. time curves. Friction coefficient is 0.8. Height of the uphill terrain is 1 m. The upper three plots correspond to the traction "control off" scenario; the lower three correspond to the traction "control on" case

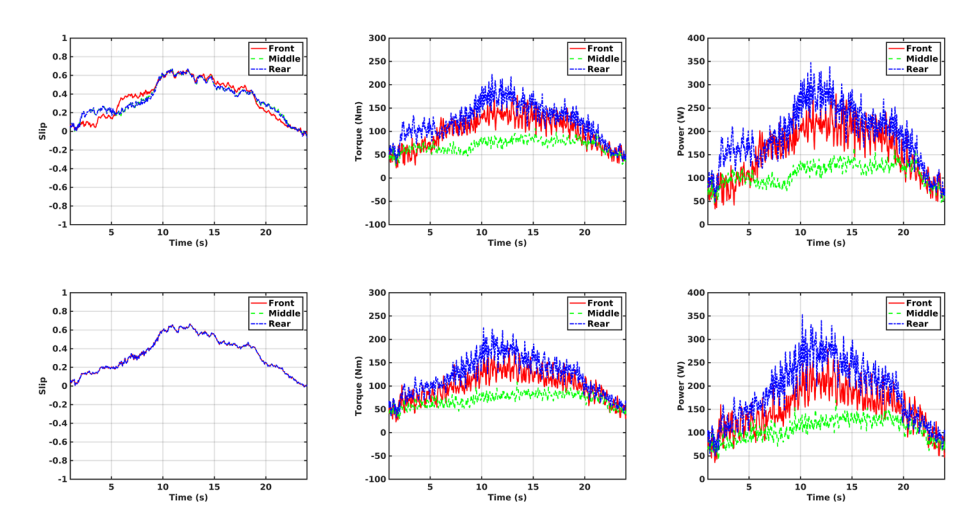


**Fig. 22** Wheel slip, torque, power vs. time curves. Friction coefficient is 0.7. Height of the uphill terrain is 1 m. The upper three plots correspond to the traction "control off" scenario; the lower three correspond to the traction "control on" case

simulations is shown in Fig. 20, which illustrates the rover position on the uphill terrain and the local particle distribution at t=15 s; the terrain height was 2 m, and the friction coefficient of the granular material was 0.9. Figure 19 and Figs. 21, 22, 23 show the time histories of the wheel slip, wheel torque, and wheel power requirement with different friction coefficients; for animations, see [60]. Figures 24, 25, 26, 27 show the time histories of the wheel slip, torque, and power requirement for different heights (H in Fig. 17); for animations, see [61]. Several points can be made in conjunction with these results: (i) The implemented traction control algorithm works fine when the friction coefficient and terrain height are changing; (ii) The lower the friction coefficient, the higher the wheel slip, yet the slip stays



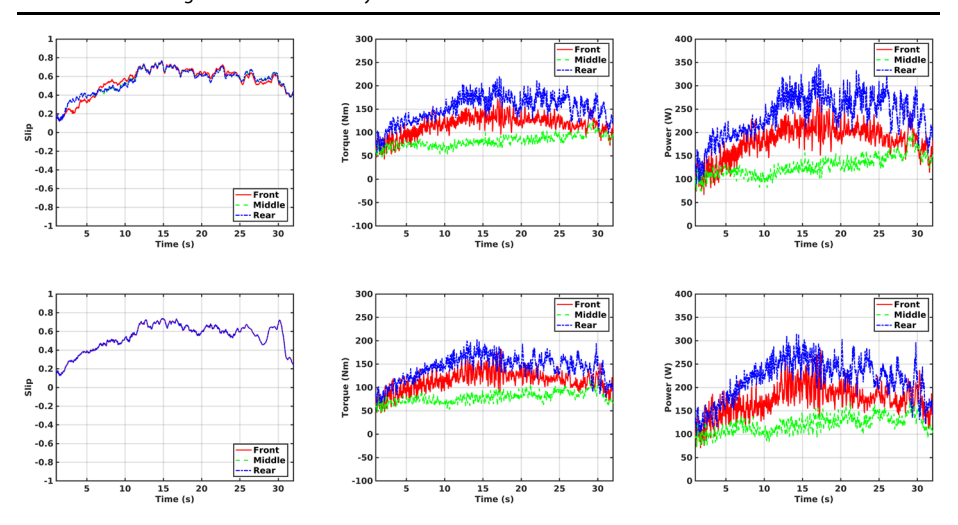


**Fig. 23** Wheel slip, torque, power vs. time curves. Friction coefficient is 0.6. Height of the uphill terrain is 1 m. The upper three plots correspond to the traction "control off" scenario; the lower three correspond to the traction "control on" case

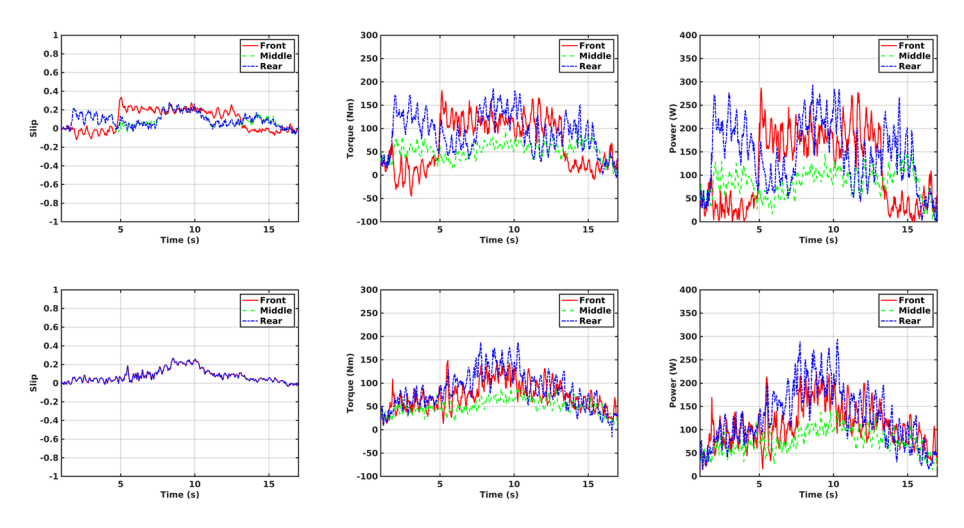


**Fig. 24** Wheel slip, torque, power vs. time curves. Friction coefficient is 0.9. Height of the uphill terrain is 1.25 m. The upper three plots correspond to the traction "control off" scenario; the lower three correspond to the traction "control on" case

roughly identical for all six wheels; (iii) A lower friction coefficient makes the rear wheels require more power and torque, whereas all across the board the middle wheels require less; (iv) Front and rear wheels require more power and torque when the terrain height increases, whereas the middle wheels keep almost constant; indeed, the middle wheels systematically play a secondary role in the overall effort.



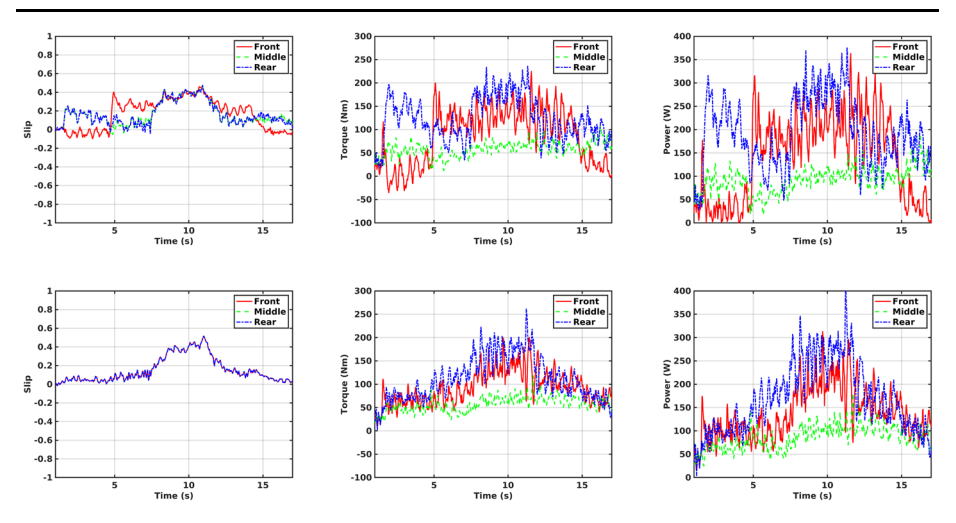


**Fig. 25** Wheel slip, torque, power vs. time curves. Friction coefficient is 0.9. Height of the uphill terrain is 1.5 m. The upper three plots correspond to the traction "control off" scenario; the lower three correspond to the traction "control on" case

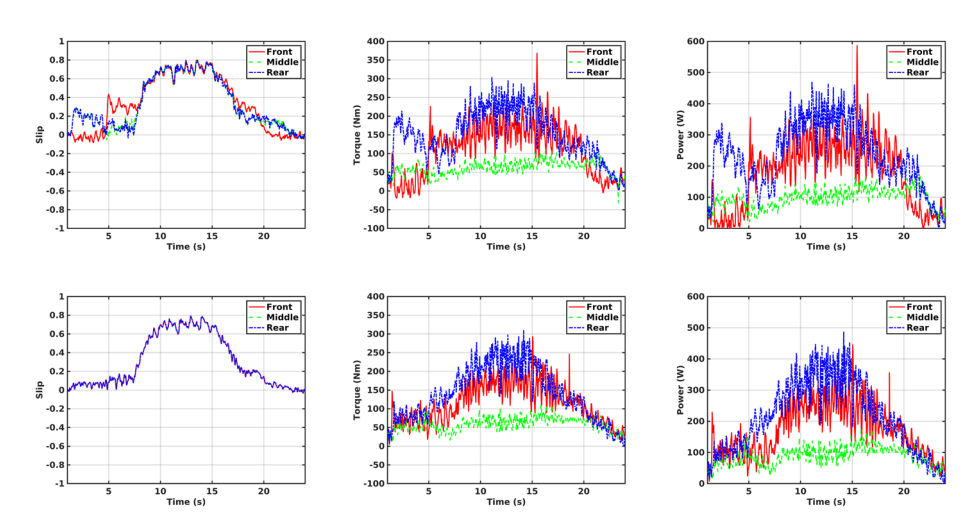


**Fig. 26** Wheel slip, torque, power vs. time curves. Friction coefficient is 0.9. Height of the uphill terrain is 1.75 m. The upper three plots correspond to the traction "control off" scenario; the lower three correspond to the traction "control on" case

#### 5 Conclusions and directions of future work

This paper outlines a computational approach that employs the SPH method to model the deformable granular material terrain and simulate its interaction with a six-wheel Curiosity Mars rover. The need for a continuum representation is motivated by the observation that a fully resolved dynamic simulation using the DEM method is prohibitively long in many practical applications [62]. By comparison, the continuum representation-based solution using the SPH method reduces the degree of freedom count of the problem and its numerical solution. A simple traction control was employed in the full rover simulation to



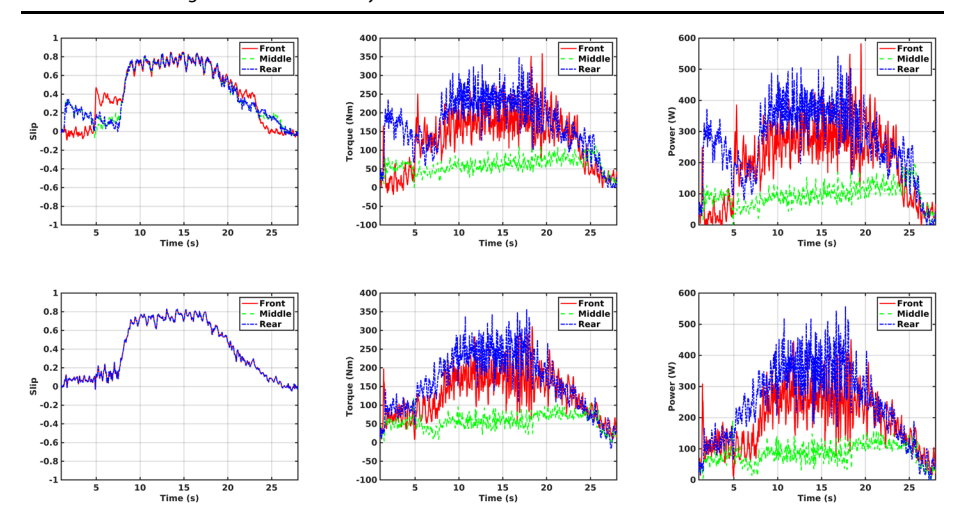


**Fig. 27** Wheel slip, torque, power vs. time curves. Friction coefficient is 0.9. Height of the uphill terrain is 2 m. The upper three plots correspond to the traction "control off" scenario; the lower three corresponds to the traction "control on" case

reduce energy usage by controlling wheel slip. As future work, it remains to understand how to handle scenarios in which the granular material departs from the monodisperse assumption, thus opening the door to more complex grain geometries. Additionally, further analytical work is required in the current approach to support mobility on snow, where there is a manifest compressibility in the material. Currently, the equations of motion work off an assumption of incompressibility, which while sufficient for sands, silts, and sand clays, fails to be adequate for snow. All the software and models used in this study are available as open source on GitHub [63] to facilitate dissemination and reproducibility studies.

**Acknowledgements** This work was supported by NASA under a Sequential STTR contract 80NSSC20C0252. Support was also provided by National Science Foundation grant CISE1835674 and US Army Research Office under grants W911NF1910431 and W911NF1810476.

#### References

- Johnson, J.B., Kulchitsky, A.V., Duvoy, P., Iagnemma, K., Senatore, C., Arvidson, R.E., Moore, J.: Discrete element method simulations of Mars exploration rover wheel performance. J. Terramech. 62, 31–40 (2015)
- Ucgul, M., Fielke, J., Saunders, C.: Three-dimensional discrete element modeling (DEM) of tillage: accounting for soil cohesion and adhesion. Biosyst. Eng. 129, 298–306 (2015)
- Zhao, C.-L., Zang, M.-Y.: Application of the FEM/DEM and alternately moving road method to the simulation of tire-sand interactions. J. Terramech. 72, 27–38 (2017)
- Recuero, A.M., Serban, R., Peterson, B., Sugiyama, H., Jayakumar, P., Negrut, D.: A high-fidelity approach for vehicle mobility simulation: nonlinear finite element tires operating on granular material. J. Terramech. 72, 39–54 (2017)
- Negrut, D., Mazhar, H.: Sand to mud to fording: modeling and simulation for off-road ground vehicle mobility analysis. In: International Workshop on Bifurcation and Degradation in Geomaterials, pp. 235–247. Springer, Berlin (2017)
- Cundall, P.A., Strack, O.D.L.: A discrete numerical model for granular assemblies. Geotechnique 29(1), 47–65 (1979)
- Bertrand, F., Leclaire, L., Levecque, G.: DEM-based models for the mixing of granular materials. Chem. Eng. Sci. 60(8–9), 2517–2531 (2005)



Longmore, J.-P., Marais, P., Kuttel, M.M.: Towards realistic and interactive sand simulation: a GPU-based framework. Powder Technol. 235, 983–1000 (2013)

- Hou, Q., Dong, K., Yu, A.: DEM study of the flow of cohesive particles in a screw feeder. Powder Technol. 256, 529–539 (2014)
- Gan, J., Zhou, Z., Yu, A.: A GPU-based DEM approach for modeling of particulate systems. Powder Technol. 301, 1172–1182 (2016)
- He, Y., Evans, T., Yu, A., Yang, R.: A GPU-based DEM for modeling large scale powder compaction with wide size distributions. Powder Technol. 333, 219–228 (2018)
- Toson, P., Siegmann, E., Trogrlic, M., Kureck, H., Khinast, J., Jajcevic, D., Doshi, P., Blackwood, D., Bonnassieux, A., Daugherity, P.D., et al.: Detailed modeling and process design of an advanced continuous powder mixer. Int. J. Pharm. 552(1–2), 288–300 (2018)
- Chauchat, J., Médale, M.: A three-dimensional numerical model for dense granular flows based on the μ (i) rheology. J. Comput. Phys. 256, 696–712 (2014)
- Ionescu, I.R., Mangeney, A., Bouchut, F., Roche, O.: Viscoplastic modeling of granular column collapse with pressure-dependent rheology. J. Non-Newton. Fluid Mech. 219, 1–18 (2015)
- Liu, G.R., Liu, M.B.: Smoothed Particle Hydrodynamics: A Meshfree Particle Method. World Scientific, Singapore (2003)
- Sulsky, D., Chen, Z., Schreyer, H.L.: A particle method for history-dependent materials. Comput. Methods Appl. Mech. Eng. 118(1–2), 179–196 (1994)
- Bardenhagen, S.G., Brackbill, J.U., Sulsky, D.: The material point method for granular materials. Comput. Methods Appl. Mech. Eng. 187(3), 529–541 (2000)
- Yue, Y., Smith, B., Chen, P.Y., Chantharayukhonthorn, M., Kamrin, K., Grinspun, E.: Hybrid grains: adaptive coupling of discrete and continuum simulations of granular media. ACM Trans. Graph. 37(6), 1–19 (2018)
- Soga, K., Alonso, E., Yerro, A., Kumar, K., Bandara, S.: Trends in large-deformation analysis of landslide mass movements with particular emphasis on the material point method. Geotechnique 66(3), 248–273 (2016)
- Baumgarten, A.S., Kamrin, K.: A general fluid–sediment mixture model and constitutive theory validated in many flow regimes. J. Fluid Mech. 861, 721–764 (2019)
- Lucy, L.B.: A numerical approach to the testing of the fission hypothesis. Astron. J. 82, 1013–1024 (1977)
- Gingold, R.A., Monaghan, J.J.: Smoothed particle hydrodynamics: theory and application to nonspherical stars. Mon. Not. R. Astron. Soc. 181(1), 375–389 (1977)
- Bui, H.H., Fukagawa, R., Sako, K., Ohno, S.: Lagrangian meshfree particles method (SPH) for large deformation and failure flows of geomaterial using elastic–plastic soil constitutive model. Int. J. Numer. Anal. Methods Geomech. 32(12), 1537–1570 (2008)
- Wei, C., Qiu, T.: Numerical simulations for large deformation of granular materials using smoothed particle hydrodynamics method. Int. J. Geomech. 12(2), 127–135 (2012)
- Nguyen, C.T., Nguyen, C.T., Bui, H.H., Nguyen, G.D., Fukagawa, R.: A new SPH-based approach to simulation of granular flows using viscous damping and stress regularisation. Landslides 14(1), 69–81 (2017)
- Hurley, R.C., Andrade, J.E.: Continuum modeling of rate-dependent granular flows in SPH. Comput. Part. Mech. 4(1), 119–130 (2017)
- Hu, W., Rakhsha, M., Yang, L., Kamrin, K., Negrut, D.: Modeling granular material dynamics and its two-way coupling with moving solid bodies using a continuum representation and the SPH method. Comput. Methods Appl. Mech. Eng. 385, 114022 (2021)
- 28. Pazouki, A., Negrut, D.: A numerical study of the effect of particle properties on the radial distribution of suspensions in pipe flow. Comput. Fluids 108, 1–12 (2015)
- Rakhsha, M., Pazouki, A., Serban, R., Negrut, D.: Using a half-implicit integration scheme for the SPH-based solution of fluid-solid interaction problems. Comput. Methods Appl. Mech. Eng. 345, 100–122 (2019)
- Hu, W., Tian, Q., Hu, H.: Dynamic simulation of liquid-filled flexible multibody systems via absolute nodal coordinate formulation and sph method. Nonlinear Dyn. 75(4), 653–671 (2014)
- Pazouki, A., Serban, R., Negrut, D.: A high performance computing approach to the simulation of fluidsolid interaction problems with rigid and flexible components. Arch. Mech. Eng. 61(2), 227–251 (2014)
- Hu, W., Tian, Q., Hu, H.: Simulating coupled dynamics of a rigid-flexible multibody system and compressible fluid. Sci. China, Phys. Mech. Astron. 61(4), 044711 (2018)
- Dunatunga, S., Kamrin, K.: Continuum modelling and simulation of granular flows through their many phases. J. Fluid Mech. 779, 483 (2015)
- Gurtin, M.E., Fried, E., Anand, L.: The Mechanics and Thermodynamics of Continua. Cambridge University Press, Cambridge (2010)



- 35. Monaghan, J.J.: SPH without a tensile instability. J. Comput. Phys. 159(2), 290-311 (2000)
- Gray, J.P., Monaghan, J.J., Swift, R.P.: SPH elastic dynamics. Comput. Methods Appl. Mech. Eng. 190(49–50), 6641–6662 (2001)
- Yue, Y., Smith, B., Batty, C., Zheng, C., Grinspun, E.: Continuum foam: a material point method for shear-dependent flows. ACM Trans. Graph. 34(5), 1–20 (2015)
- 38. Monaghan, J.J.: Smoothed particle hydrodynamics, Rep. Prog. Phys. 68(1), 1703–1759 (2005)
- Fatehi, R., Manzari, M.T.: Error estimation in smoothed particle hydrodynamics and a new scheme for second derivatives. Comput. Math. Appl. 61(2), 482–498 (2011)
- Trask, N., Maxey, M., Kimb, K., Perego, M., Parks, M.L., Yang, K., Xu, J.: A scalable consistent secondorder SPH solver for unsteady low Reynolds number flows. Comput. Methods Appl. Mech. Eng. 289, 155–178 (2015)
- Pan, W., Kim, K., Perego, M., Tartakovsky, A.M., Parks, M.L.: Modeling electrokinetic flows by consistent implicit incompressible smoothed particle hydrodynamics. J. Comput. Phys. 334, 125–144 (2017)
- 42. Hu, W., Pan, W., Rakhsha, M., Tian, Q., Hu, H., Negrut, D.: A consistent multi-resolution smoothed particle hydrodynamics method. Comput. Methods Appl. Mech. Eng. **324**, 278–299 (2017)
- Hu, W., Guo, G., Hu, X., Negrut, D., Xu, Z., Pan, W.: A consistent spatially adaptive smoothed particle hydrodynamics method for fluid-structure interactions. Comput. Methods Appl. Mech. Eng. 347, 402–424 (2019)
- Bonet, J., Lok, T.-S.L.: Variational and momentum preservation aspects of smooth particle hydrodynamic formulations. Comput. Methods Appl. Mech. Eng. 180(1–2), 97–115 (1999)
- 45. Takeda, H., Miyama, S.M., Sekiya, M.: Numerical simulation of viscous flow by smoothed particle hydrodynamics. Prog. Theor. Phys. **92**(5), 939–960 (1994)
- Morris, J.P., Fox, P.J., Zhu, Y.: Modeling low Reynolds number incompressible flows using SPH. J. Comput. Phys. 136(1), 214–226 (1997)
- Holmes, D.W., Williams, J.R., Tilke, P.: Smooth particle hydrodynamics simulations of low Reynolds number flows through porous media. Int. J. Numer. Anal. Methods Geomech. 35(4), 419–437 (2011)
- Zhan, L., Peng, C., Zhang, B., Wu, W.: Three-dimensional modeling of granular flow impact on rigid and deformable structures. Comput. Geotech. 112, 257–271 (2019)
- Bian, X., Ellero, M.: A splitting integration scheme for the SPH simulation of concentrated particle suspensions. Comput. Phys. Commun. 185(1), 53–62 (2014)
- 50. Monaghan, J.J.: On the problem of penetration in particle methods. J. Comput. Phys. 82(1), 1–15 (1989)
- 51. Monaghan, J.J.: Simulating free surface flows with SPH. J. Comput. Phys. 110, 399 (1994)
- Xu, R., Stansby, P., Laurence, D.: Accuracy and stability in incompressible SPH (ISPH) based on the projection method and a new approach. J. Comput. Phys. 228(18), 6703–6725 (2009)
- Pazouki, A., Kwarta, M., Williams, K., Likos, W., Serban, R., Jayakumar, P., Negrut, D.: Compliant versus rigid contact: a comparison in the context of granular dynamics. Phys. Rev. E 96, 042905 (2017)
- Negrut, D., Serban, R., Tasora, A.: Posing multibody dynamics with friction and contact as a differential complementarity problem. ASME J. Comput. Nonlinear Dyn. 13(1), 014503 (2017)
- Melanz, D., Jayakumar, P., Negrut, D.: Experimental validation of a differential variational inequalitybased approach for handling friction and contact in vehicle/granular-terrain interaction. J. Terramech. 65, 1–13 (2016)
- Brian Kumanchik, NASA, and JPL-Caltech: Curiosity clean,nasa 3d resources (2016). https://nasa3d.arc.nasa.gov/detail/curiosity-clean
- Gutierrez, F., Ricchio, C., Rakhsha, M., Pazouki, A., Hu, W., Negrut, D.: Investigation of mesh to point cloud conversion approaches for applications in SPH-based fluid-solid interaction simulations. Technical Report TR-2015-10, Simulation-Based Engineering Laboratory, University of Wisconsin-Madison (2015)
- Fraeman, A.: The rocks vs. stone cold aluminum wheels (2018). https://mars.nasa.gov/MSL/mission/mars-rover-curiosity-mission-updates/index.cfm?mu=sol-2032-2033-the-rocks-vs-stone-cold-aluminum-wheels
- Toupet, O., Biesiadecki, J., Rankin, A., Steffy, A., Meirion-Griffith, G., Levine, D., Schadegg, M., Maimone, M.: Traction control design and integration onboard the Mars science laboratory Curiosity rover. In: 2018 IEEE Aerospace Conference, pp. 1–20 (2018)
- Hu, W., Zhou, J., Negrut, D.: Mobility simulations of Mars Curiosity rover with traction control on uphill granular material terrain with different friction. Simulation-Based Engineering Laboratory, University of Wisconsin Press-Madison, 2021. https://uwmadison.box.com/s/gszprtae2tbfnv70xbms33wm1pxfnvui
- Hu, W., Zhou, J., Negrut, D.: Mobility simulations of Mars Curiosity rover with traction control on uphill granular material terrain with different heights. Simulation-Based Engineering Laboratory, University of Wisconsin Press-Madison, 2021. https://uwmadison.box.com/s/as31kohnxj3cw6l9cre99zrwu9b9da6n
- Kelly, C., Olsen, N., Negrut, D.: Billion degree of freedom granular dynamics simulation on commodity hardware via heterogeneous data-type representation. Multibody Syst. Dyn. 50, 355–379 (2020)



Chrono Project Development Team: Chrono: an Open Source Framework for the Physics-Based Simulation of Dynamic Systems. <a href="https://github.com/projectchrono/chrono">https://github.com/projectchrono/chrono</a>. Accessed: 2019-12-07

**Publisher's Note** Springer Nature remains neutral with regard to jurisdictional claims in published maps and institutional affiliations.

#### **Authors and Affiliations**

Wei Hu<sup>1</sup> • Zhenhao Zhou<sup>1</sup> • Samuel Chandler<sup>2</sup> • Dimitrios Apostolopoulos<sup>2</sup> • Ken Kamrin<sup>3</sup> • Radu Serban<sup>1</sup> • Dan Negrut<sup>1</sup> •

D. Negrut

negrut@wisc.edu

W. Hu

whu59@wisc.edu

Z. Zhou

zzhou292@wisc.edu

S. Chandler

samxchandler@protoinnovations.com

D. Apostolopoulos

da1v@protoinnovations.com

K. Kamrin

kkamrin@mit.edu

R. Serban

serban@wisc.edu

- Department of Mechanical Engineering, University of Wisconsin-Madison, Madison, WI 53706, USA
- ProtoInnovations, LLC, Pittsburgh, PA 15201, USA
- Department of Mechanical Engineering, Massachusetts Institute of Technology, Cambridge, MA 02139, USA

